Exploiting the Terahertz Band for Radionavigation

John Scott Parker, *Tufts University*
Pascal Mickelson, *PM&AM Research*
Jeremy Yeak, *PM&AM Research*
Kevin Kremeyer, *PM&AM Research*
Jason Rife, *Tufts University*

Accepted to Journal of Infrared, Millimeter and Terahertz Waves, June 2016
Pre-print version.

For published paper visit:
http://rdcu.be/jYOI
Or
http://link.springer.com/article/10.1007/s10762-016-0291-8

Exploiting the Terahertz Band for Radionavigation

John Scott Parker, ***Tufts University***
Pascal Mickelson, ***PM&AM Research***
Jeremy Yeak, ***PM&AM Research***
Kevin Kremeyer, ***PM&AM Research***
Jason Rife, ***Tufts University***

Primary Contact
John Scott Parker
Department of Mechanical Engineering
200 College Ave
Medford, MA 02155
John_S.Parker@Tufts.edu
617-780-9680

Abstract This paper demonstrates the feasibility of GPS-like ranging at terahertz (THz) frequencies. It is well established that GPS carrier signals are vulnerable to jamming via Radio-Frequency Interference (RFI). As a result, there is a need for alternative radionavigation systems. THz signals offer a compelling option. Because of their high frequency (roughly 100x higher than GPS), THz signals can be used to make highly precise range measurements. In addition, the large separation between the GPS and THz frequencies means that interference at GPS frequencies is very unlikely to impact the THz band. This paper lays the groundwork for a GPS-like ranging capability at THz frequencies. To this end, we identify key differences between THz hardware and GPS (radio frequency) hardware; we experimentally evaluate performance of a 0.30 THz system on a compact outdoor test range; and we introduce a measurement error model that highlights the distinctive role that multipath interference plays at THz frequencies.

Keywords: ranging, time-of-flight, multipath, link budget, GPS alternative

Work supported by the AFRL through contract FA8650-12-C-3204.

Exploiting the Terahertz Band for Radionavigation

John Scott Parker • Pascal Mickelson • Jeremy Yeak • Kevin Kremeyer • Jason Rife

Abstract This paper demonstrates the feasibility of GPS-like ranging at terahertz (THz) frequencies. It is well established that GPS carrier signals are vulnerable to jamming via Radio-Frequency Interference (RFI). As a result, there is a need for alternative radionavigation systems. THz signals offer a compelling option. Because of their high frequency (roughly 100x higher than GPS), THz signals can be used to make highly precise range measurements. In addition, the large separation between the GPS and THz frequencies means that interference at GPS frequencies is very unlikely to impact the THz band. This paper lays the groundwork for a GPS-like ranging capability at THz frequencies. To this end, we identify key differences between THz hardware and GPS (radio frequency) hardware; we experimentally evaluate performance of a 0.30 THz system on a compact outdoor test range; and we introduce a measurement error model that highlights the distinctive role that multipath interference places at THz frequencies.

Keywords: ranging, time-of-flight, multipath, link budget, GPS alternative

1 Introduction

GPS has revolutionized position finding and stimulated innovations in a wide range of fields—including surveying, geology, farming, robotics, and aviation—which have contributed as much as $100 billion to the U.S. economy [1]. It is well-established, however, that GPS suffers from a critical vulnerability: its susceptibility to jamming by Radio-Frequency Interference (RFI) [2,3]. As a result, there is demand for GPS alternatives [4,5], particularly ones that are robust to interference at GPS frequencies.

Terahertz-frequency (THz) communications are an emerging field of study with a variety of potential applications including ranging and navigation [6,7]. Because of their high frequencies (at least two orders of magnitude greater than GPS), THz signals have the potential to provide extremely high-accuracy distance measurements using carrier methods [8,9] to yield derivative range and position information. In addition, the large frequency difference between THz and GPS carrier signals means that interference at GPS frequencies is very unlikely to have an impact on THz hardware. This feature makes THz frequencies a compelling alternative to GPS frequencies for ranging applications that may be otherwise vulnerable to interference.

THz radiation lies between microwaves and infrared radiation on the electromagnetic spectrum, roughly between 0.3 THz and 10 THz [10,11], as shown in **Fig. 1**. This band is often referred to as the "THz gap," because of its historical difficulty to exploit. It marks the transition between optical and electronic frequencies, which each utilize very different hardware [12]. Adapting technology from these neighboring bands to work at THz frequencies has proven difficult. In addition, THz frequencies are absorbed by atmospheric gases, so signal attenuation can be significant near ground level, especially for frequencies at the higher end of the band [13]. As a result, the development of affordable THz hardware has been slow.

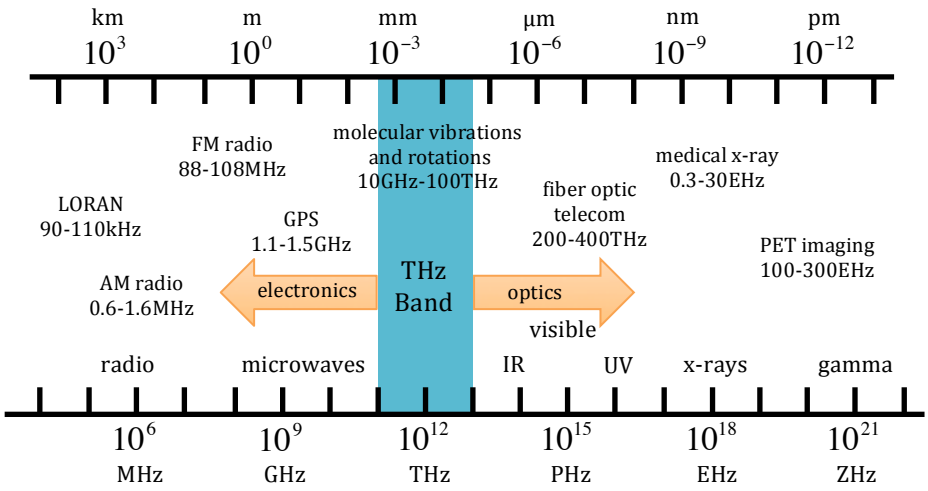

Fig. 1 The THz band lies at the intersection of optical and electronic frequencies in the electromagnetic spectrum

Despite these limitations, interest in THz technology has grown significantly in recent years as the demands for high-speed wireless communications increase and unoccupied frequency bands are gobbled up. Technological advances have started to close the "THz gap" over the last decade or so [14], and THz transmitters and receivers have recently become commercially available [15,16]. With the increasing availability of hardware, researchers are now using THz signals for a wide variety of applications, including medical imaging of tumors [17], non-destructive paint and enamel thickness evaluation [18], remote sensing radar [19–21], airport security scanning [22], and wireless indoor communications [23–28]. THz positioning and navigation research has thus far consisted primarily of work on radar-like methods, which are inherently range limited due to spreading losses following signals reflection [29,30].

This paper takes a fundamentally different approach to THz positioning and navigation; one that lays the groundwork for a GPS-like ranging capability that would function over significantly longer distances than a radar-like capability. To demonstrate the feasibility of GPS-like ranging using THz frequencies, this paper describes three key results. First, we discuss THz hardware implementation and identify relevant differences from conventional GPS hardware, which operates at radio frequencies. Next we demonstrate feasibility by presenting experimental results of our hardware system's performance on a compact outdoor test range. Lastly, we introduce a model for THz range-measurement error with an emphasis on multipath, since multipath plays a somewhat different role in THz-ranging systems as compared to conventional radio-frequency ranging systems. Simulations based on our error models suggest the potential for obtaining ranging measurements over baselines of several kilometers.

The paper begins by describing the THz equipment and algorithms used in our experiments. Next, the experimental results are discussed, and models of measurement error are developed. A discussion section uses the error models to predict ranging accuracy over an extended baseline. The paper concludes with a brief summary.

2 Experimental Hardware

Similar to GPS, our THz ranging system works by measuring the signal's time-of-flight. The time-of-flight t_{TOF} is simply the difference between the time the signal leaves transmitter t_t and the time the signal reaches the receiver t_r

$$t_{TOF} = t_r - t_t. \tag{1}$$

Because the signal travels at the speed of light, the distance r between the transmitter and receiver is equal to the time-of-flight t_{TOF} multiplied by the speed of light c

$$r = ct_{TOF}. \tag{2}$$

Time-of-flight measurements were made using proprietary hardware developed by PM&AM, LLC (Tucson, AZ). A simplified block diagram for the hardware is shown in **Fig. 2**. The transmitter hardware is illustrated on the left of the figure, and the receiver hardware on the right.

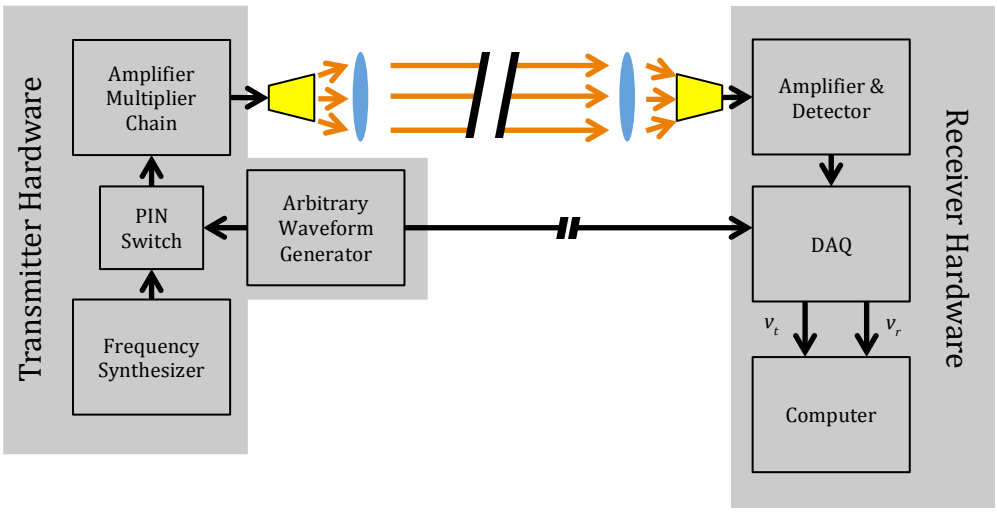

Fig. 2 Simplified system block diagram showing the main components of the transmitter and receiver hardware

This system differs from previously published THz ranging systems [19–21,29,30], which use radar methods to measure the range. Modeled on GPS, the transmitter and receiver are placed at opposite ends. This significantly reduces transmission losses as compared to radar methods, because the signal travels half as far and does not require a reflection. In addition, it makes it possible for a standalone receiver to measure range and perform trilateration position estimation, as in GPS.

The remainder of this section provides a rough overview of the transmitter equipment, the receiver equipment, and the ground-truth system used in subsequent experiments.

2.1 Transmitter

The primary components of the transmitter are a tunable frequency synthesizer and an amplifier-multiplier chain (AMC). In this system, the base frequency generated by the synthesizer is increased by a factor of 24 going through the AMC. For example, to generate 300 GHz (0.3 THz), the output of the tunable frequency synthesizer is set to 12.5 GHz so that after the AMC, a carrier frequency of 12.5 GHz x 24 = 300 GHz is obtained.

Simple on-off keying is applied to modulate the carrier signal. An arbitrary waveform generator controls a PIN switch with 200 ps rise/fall time, which toggles the transmitter on and off. In addition to controlling the PIN switch, the output of the waveform generator is used to trigger data collection on the personal computer.

Although the waveform generator will eventually be used to modulate a pseudo-random code sequence onto the THz carrier, the modulation in the following experiments was a simple 10 MHz square wave. The modulated signal has a period of 100 ns and a wavelength of 30 m, as illustrated in **Fig. 3**.

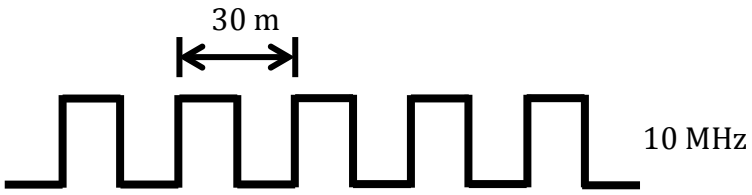

Fig. 3 The THz signal is modulated with a 10 MHz square wave using simple on-off modulation

The assembled transmitter has an output power greater than 30 mW in the 300-325 GHz band. At the output of the transmitter, a diagonal horn antenna is used to transmit the 300-GHz carrier wave. To decrease spreading losses, a Teflon lens is used to partially collimate the beam, resulting in a signal divergence of roughly 2.5° (we reasonably treat the transmitter hardware as a point source in the following analysis).

The key difference between the THz transmitter and RF transmitters used in GPS is the modulation of the carrier signal. Ideally, binary phase-shift keying (BPSK) would be used to modulate code onto the THz carrier

signal, as in GPS; however, as described below, current hardware limitations make carrier-phase tracking impossible. As a result, simple on-off modulation is used.

2.2 Receiver

The receiver equipment consists of an analog front end that demodulates the received signal. A data acquisition system digitizes the demodulated signal and sends it to a personal computer.

The first stage of the front end is a Teflon lens that concentrates the received signal on a 25-dB gain diagonal horn antenna. The beam divergence of the lens/antenna assembly is roughly 4°, and the lens area is 4.9×10^{-5} m^2. Attached to the antenna are a series of low-noise amplifiers that feed into a 300-330 GHz zero-bias Schottky-diode direct detector. The detector rectifies and accumulates the received signal. Rectification results in demodulation, mixing half the power in the THz signal down to the baseband, centered at DC (and the other half of the power to twice the carrier frequency). The accumulation process acts likes a low-pass filter stage, with a bandwidth of approximately 1 GHz. In the process of accumulation, only the baseband signal is preserved. All higher-frequency data (e.g. carrier phase data) is lost during accumulation. The output of the detector is fed to a data acquisition system (DAQ), where an A/D converter digitizes the detector output at a sample rate of 1 GSample/Sec.

In order to determine range from time-of-flight, the DAQ sends the detector output to the personal computer for storage and post processing. The DAQ also digitizes the waveform generator output, which is used to create the transmitted signal. In this manner, the detector and waveform generator outputs were both tagged with a common clock at the data-acquisition computer. The transmission and line delays were calibrated to correct the time-of-flight measurement (see below). Some residual clock error persists, where that error is a fraction of the DAQ's temporal resolution (e.g., a fraction of 1 ns).

As noted, the key difference between the THz and GPS receivers is their ability to track the phase of the carrier signal. Although this capability will likely be available in the future, currently affordable THz receivers rectify and accumulate the signal, resulting in a loss of carrier phase data. This prevents the use of BPSK on the THz carrier signal, as in GPS.

2.3 Ground Truth System

Ground truth was obtained by taking physical distance measurements (using a tape measure), in order to provide a basis of comparison for the ranging measurements obtained from the THz system.

In order to allow for variable separation between receiver and transmitter hardware, both units were placed on separate mobile carts. The equipment was mounted on the carts approximately 1 m above the ground. The receiver cart was equipped with an uninterruptible power supply that allowed the operation of the receiver for over 8 hours without being tethered to a wall plug. Due to its higher power demands, the transmitter cart was powered via a wall plug. The separation between the transmitter and receiver carts was measured using markings on the ground, which were surveyed with a tape measure prior to the start of experimental data collection.

3 Range Measurement Methods

The objective of the experimental system is to precisely measure the signal's time-of-flight so that the range can be determined accurately via Eq. (2). A code-phase-based method was used to compare the offset between the transmitted and received signal (as described above, carrier-phase information is lost in signal rectification, so only code-phase is available for processing). The basic concept is to compare the received signal to the transmitted signal in order to determine the delay caused by the time-of-flight. The received signal should be delayed as compared to the transmitted signal, so finding the range entails finding the phase delay of the modulated signal (assuming that equipment delays have already been accounted for via the calibration described below), as illustrated in **Fig. 4**. In the case shown, the phase difference between the received and transmitted signals is 0.7 cycles. The 10 MHz modulation signal has a period of 100 ns corresponding to a wavelength of $\lambda = 30$ m, so if the phase shift between the transmitter signal and the receiver signal is $\theta_r - \theta_t = 0.7$, the distance between transmitter and receiver is $(\theta_r - \theta_t)\lambda = 21$ m.

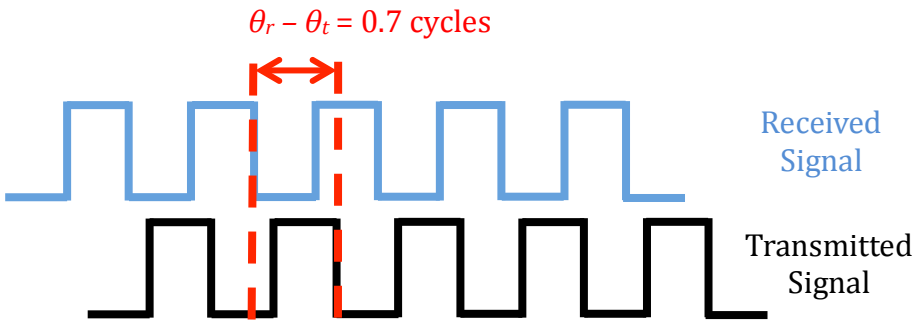

Fig. 4 In this example of phase-angle ranging, the measured phase difference is $\theta_r - \theta_t = 0.7$ cycles. For a 10 MHz signal with a wavelength $\lambda = 30$ m, that means that the measured range between the transmitter and receiver is $\theta_r - \theta_t = 21$ m

It should be noted that range measurements obtained in this way are subject to a cycle ambiguity since all chips have the same form. Because of the repetitive nature of the signal, it is impossible to tell the difference between a phase shift of 0.7 cycles and one of 1.7 cycles, 2.7 cycles, *etc*. For the purposes of this experiment, ambiguities were resolved procedurally, as described below (rather than via signal processing as, for example, in GPS).

To simplify signal processing, the phase shift was related to time-of-flight using only the fundamental frequency. The fundamental frequency is the sine wave at the same frequency as the transmitted square wave. Decomposing the square wave sequence into a Fourier Series, the voltage component associated with the fundamental frequency is a sinusoidal wave at $\omega/2\pi = 10$ MHz. For this sinusoidal wave, the phase shift can be related to time-of-flight t_{TOF} from Eqs. (1) and (2) as

$$t_{TOF}(k) = \frac{1}{\omega}(\theta_r(k) - \theta_t(k) + 2\pi M) - \delta + n, \tag{3}$$

where k is the time step (with $t(k) = k\tau$ where τ is the sample period of 1 ns), θ_r is the received-signal phase shift and θ_t is the transmitted-signal phase shift (both are defined relative to the arbitrary clock reference), M is the cycle ambiguity, which is an arbitrary integer, δ represents the cable and hardware delays, and n a random variable representing corruption of the time-of-flight measurement by thermal noise and multipath.

Because the clock reference is common to the received and transmitted signals, the time reference can be set arbitrarily to zero at the midpoint of the first chip. The analytic expression v_t for the fundamental-frequency component of the transmitted signal voltage is given by

$$v_t = \cos(\omega t). \tag{4}$$

Higher harmonic frequencies were not tracked in our experiments, so we will consider only the fundamental frequency here.

The fundamental frequency of the received signal is assumed to match that of the transmitted signal, as Doppler shift was assumed to be negligible for all experiments. Thus, the voltage v_r associated with the fundamental frequency of the received signal is modeled to be

$$v_r = \cos\big(\omega(t - t_{TOF} - \delta + n)\big). \tag{5}$$

A very simple means of extracting the phase shift at the fundamental frequency from the raw (square-wave) data is to correlate both transmitted and received signals with a complex sinusoid at the fundamental frequency. This procedure extracts the in-phase and quadrature components of the signal. The correlation operation was performed in software after digitization of the signals from the waveform generator (transmitter signal) and the detector (receiver signal). These correlations were performed over a sliding window of K data points, as described by the following equation. The in-phase and quadrature correlations at a particular time step k, labeled $I(k)$ and $Q(k)$ respectively, are equivalent to discrete cosine and sine transforms at the fundamental frequency

$$I_i(k) = \sum_{m=k-K+1}^{k} \cos(\omega m\tau) v_i(m) \quad \text{and} \tag{6}$$

$$Q_i(k) = \sum_{m=k-K+1}^{k} \sin(\omega m\tau) v_i(m). \tag{7}$$

The same correlation operation was applied to both the transmitted and received waveforms, hence the index i is used here to refer generically to either the transmitted or received signal, such that $v_i = \{v_t, v_r\}$ from Eqs. (4) and (5).

The in-phase and quadrature signals can be combined to compute a phase angle at each time step as follows,

$$\theta_i(k) = \text{atan}^{-1}\left(\frac{-Q_i(k)}{I_i(k)}\right). \tag{8}$$

The transmitted signal phase θ_t and received signal phase θ_r were obtained by applying Eqs. (6), (7) and (8) separately to the transmitted and received waveforms v_t and v_r. Finally, the time-of-flight is computed by substituting these values of θ_t and θ_r into the time-of-flight equation, given by Eq. (3).

An example correlation is shown in **Fig. 5**, for a small sample set of receiver data collected at an equipment separation of 4 m. The raw voltage measurements that make up the received signal v_r, shown in blue, form a square wave corrupted by noise. The on-off transitions of the square wave are clearly visible at 4 m separation. The purpose of the correlators from Eqs. (6) and (7) is to extract phase even when the transitions are not visible to the eye (as occurs at larger separation distances). The correlation function $\cos(\omega t + \theta_r)$, shown in red, is a sinusoid at the fundamental frequency of modulation. In this case, the received signal's phase θ_r is roughly 290° as computed from Eq. (8), meaning the signal v_r is shifted by 290° as compared to the reference v_t. Assuming that the transmitted signal's phase is $\theta_t = 0°$, the ambiguity is $M = 0$, and the delay δ due to transmission through the cables and hardware is known to be 67 ns, by Eq. (3) the time-of-flight t_{TOF} is 13.6 ns. Multiplying by the speed of light c, this gives a measured distance in this example of 4.07 m. It should be noted that only 300 samples are shown here for simplicity, whereas a window size of $K = 450{,}000$ samples is used in the experiments described below.

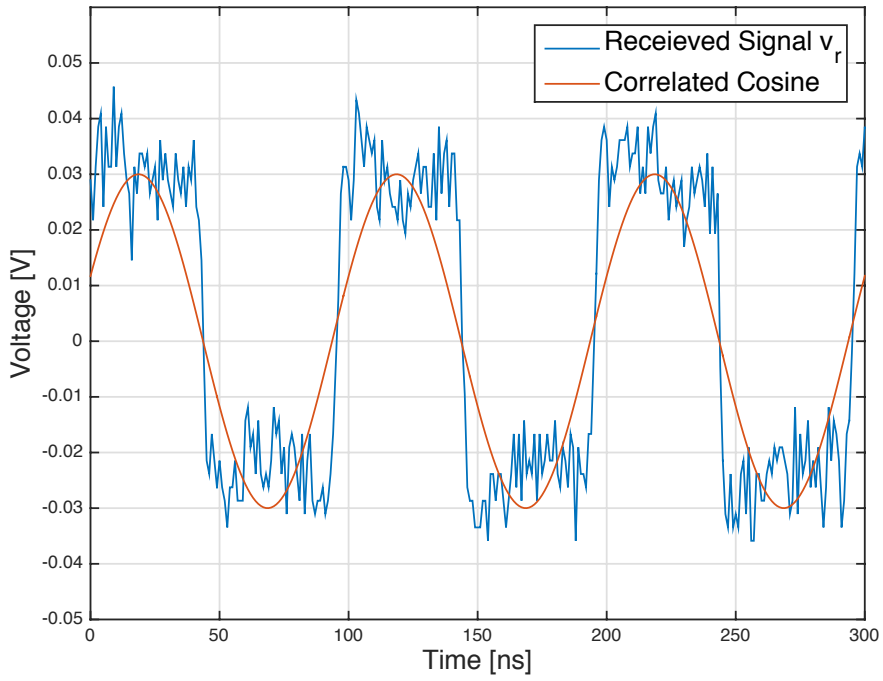

Fig. 5 An example correlation applied to a sample signal v_r received from a transmitter 4 m away.

There are a couple of important differences between this THz system and GPS systems. First, for simplicity in this demonstration, simple square wave modulation is used; however, more complex pseudorandom codes, like those used in GPS, could readily be applied to the input signal from the arbitrary waveform generator. Second, for demonstration purposes, this system uses a single clock in the DAQ tethered to both the transmitter and receiver as the time basis for measuring the delay caused by the signal's time-of-flight. The tether could be cut in one of two ways: either both the transmitter and receiver could both be equipped with synchronized atomic clocks, or, as in GPS, measurements from a constellation of four or more transmitters, each equipped with synchronized atomic clocks, could be used by the receiver to estimate the three position coordinates as well as the unknown time coordinate.

3.1 Ambiguity Resolution

For expediency, the ambiguity M in Eq. (3) was resolved manually. By starting the transmitter cart adjacent to the receiver cart, the initial ambiguity was known to be zero. In subsequent testing, when the receiver cart was slowly pulled away from the transmitter, jumps appeared in the phase measurements at each integer transition. These jumps were removed manually in post-processing so that θ_r was obtained as an accumulated phase (rather than an absolute phase angle).

Automatic resolution of the integer ambiguity will be possible in the future when the square wave signal is replaced with a pseudorandom code sequence. This implementation detail has been left to future work.

3.2 Calibration

Prior to experimental trials, a calibration procedure was performed to estimate the equipment delay δ. This was achieved by comparing a THz range measurement to a ground truth measurement at a short distance, where the signal-to-noise ratio is high. The calibration procedure is as follows:

1. Position the transmitter and receiver close to each other
2. Make time-of-flight measurement t_{TOF} using THz equipment and Eqs. (3)-(8)
3. Make independent ground truth measurement and determine expected time-of-flight $t_{TOF,ex}$ based on the speed of light c using Eq. (2)
4. Compare THz and ground truth measurements to determine offset δ using the following equation

$$\delta = t_{TOF} - t_{TOF,ex} \tag{9}$$

The delay δ is stable over the length of a test (5-10 minutes), but appeared to have variability of roughly 1 ns (up to 30 cm) over the course of days. An average value of δ (equal to 69 ns) is used in all subsequent analysis, and then a detrend process is applied to remove any residual bias from the specific data set. This is done by finding the mean error (bias) for short-range measurements (2-30 m), where ground-bounce multipath error is not a factor, and subtracting that bias from each measurement in the data set.

4 Experimental Results

Experiments were conducted at the outdoor facilities of PM&AM Research, LLC in Tucson, AZ. Results are presented for static and dynamic tests. In static tests, measurements were made with transmitter and receiver held stationary. In dynamic tests, measurements were made while range was continuously changed. The atmospheric conditions during these experiments were as follows: 103 ^{o}F (39.4 °C, 313 K), 6% relative humidity, 923 millibars (92,300 Pa), and a dew point of 25.5 ^{o}F (-3.6 °C, 270 K). Though the measurements were made at ground level, it should be noted that the local terrain was at 2500 ft (762 m) above sea level.

4.1 Thermal Noise Measurement

The noise spectral power N_0 was not well characterized for the experimental system, and so it was necessary to use experimental data to evaluate this parameter for use in the range error model developed in the following section. Noise was assessed by running the experimental system at a short range (4 m), where multipath was expected to be negligible. At this range, the receiver data were digitized and a power spectrum was evaluated using $K = 450{,}000$

points. Note that exactly 100 data points were captured over each wavelength of the 10 MHz fundamental frequency, and that K is an integer multiple of this period. The power spectra at 4 m range are shown in **Fig. 6**. Power is plotted on the vertical axis in arbitrary units and the frequency is shown along the horizontal axis in hertz. The plot on the left shows the power magnitude for the half spectrum through the Nyquist frequency (at 500 MHz). The plot on the right zooms in on the fundamental frequency and first harmonic (the range 5-25 MHz).

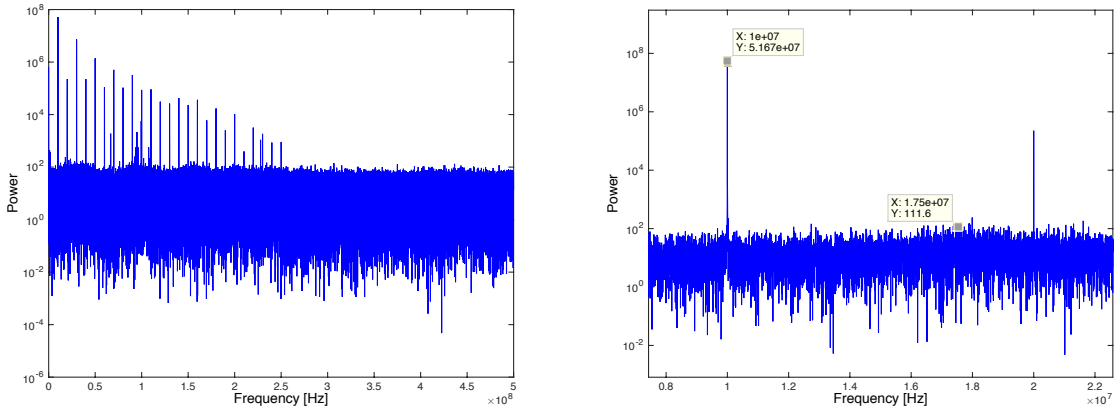

Fig. 6 Signal power over a wide range of frequencies (left) and zoomed in on the main peak at 10 MHz (right)

The figures confirm that the noise spectrum is essentially flat, justifying the assumption that thermal noise is white. Code C and noise N were obtained in the right hand plot (with values of $C = 5.2{\times}10^7$ and $N = 110$, in arbitrary units). Taking multipath to be zero at this range, the ratio of these two values can be used to estimate C/N. Evaluating C_d at 4 m from Eq. (12), as described below, it is possible to estimate N from the data, and hence to estimate N_0 from Eq. (13). The resulting value of the N_0 parameter is listed in **Table 1**.

4.2 Range Error from Static Tests

Static tests are so named because neither the transmitter nor the receiver carts were moving relative to one another. The advantages of static tests are two-fold: first, because the carts are not moving, the range between the transmitter and receiver (i.e. the ground truth measurement) can be determined precisely using a tape measure. Second, multiple data points can be recorded to assess the spread of range estimates around each transmitter-receiver separation.

In static tests, the transmitter and receiver carts were set up so that the antennas were approximately aligned. Experiments were run at several fixed distances of roughly 1 m, 10 m, 20 m, and every subsequent 10 m interval out to 100 m. The results of these static range measurements are shown in **Fig. 7**. The THz measurement errors, relative to the ground truth, are plotted in blue as a function of the true transmitter-receiver separation. To provide context, the figure also shows two types of one-sigma error bound: one without multipath (black line) and one with multipath (gray box). These models will be introduced and discussed in more detail in Section 5.

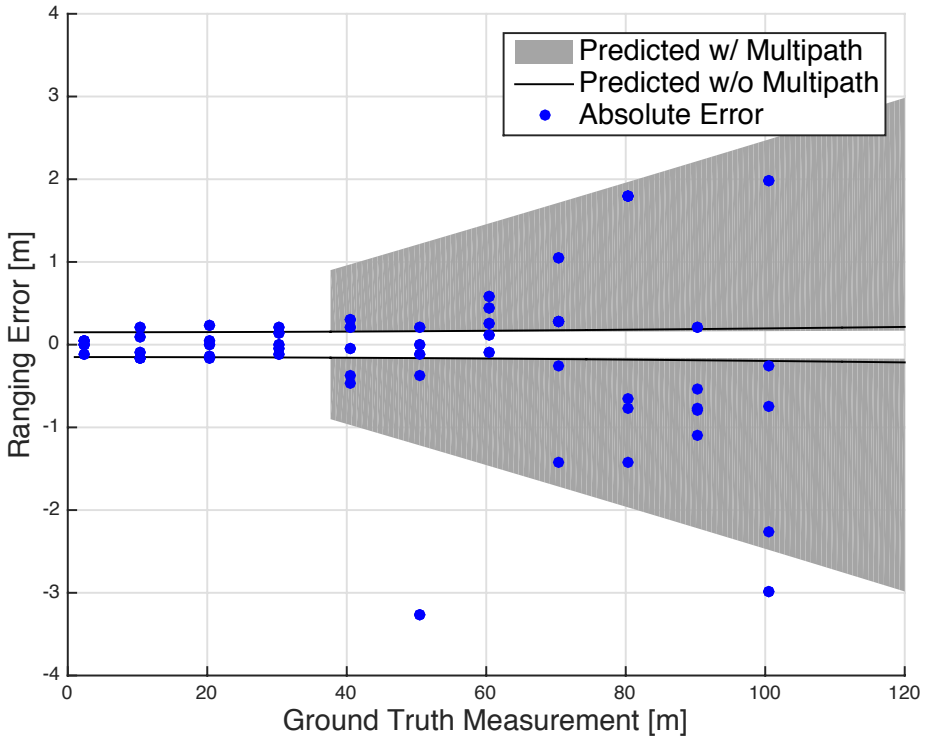

Fig. 7 Range measurement error for the static trial, where the line represents the predicted one-sigma error with no multipath interference, and the shaded region represents all of the possible one-sigma errors given multipath interference

4.3 Dynamic Tests

In contrast to static tests, dynamic tests involved moving the receiver cart continuously over the entire range of interest. While the receiver cart was manually pulled away from the transmitter, data were recorded to the computer RAM in real time. The transmitted and received signals were periodically stored to disk. In the trial, the receiver cart covered a distance of almost 100 m over the course of 200 s, at roughly constant speed (~0.5 m/s).

Concurrently, the ground truth measurements were logged independently of the THz measurements using distance markers on the ground and a stopwatch. Each time the receiver cart passed one of the distance markers, the stopwatch lap timer was used to record the time that has elapsed since the previous marker. While there is some timing error associated with this low-tech solution, the receiver moved slowly enough that the resulting record of position versus time was sufficiently accurate to provide a good ground truth for the THz ranging system.

Fig. 8 shows the results from this trial. The cart was initially stationary, and then began moving at roughly constant speed over the length of the test range before coming to a stop at the end. The THz ranges are plotted as blue circles, while the ground truth is plotted as a red line. A linear spline is used to interpolate a continuous ground truth model from the set of ground marker and lap time pairs.

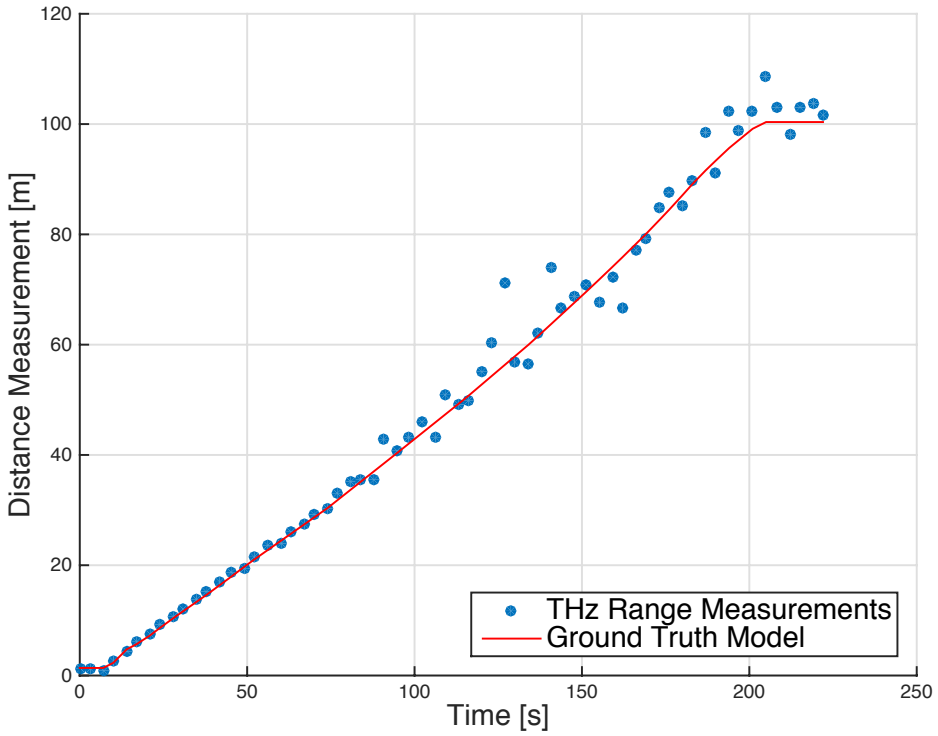

Fig. 8 Time series range measurements for the dynamic trial, where THz measurements are shown as dots and the ground truth measurements are shown as a line

The measurement residuals (measurement minus ground truth model) are plotted in **Fig. 9**. Individual ranging error measurements are shown as blue circles, and the one-sigma error bounds are again shown in black with the gray boxes indicating the uncertainty once multipath signals come into play. It should be noted that the errors in this trial are significantly higher than in the static trial.

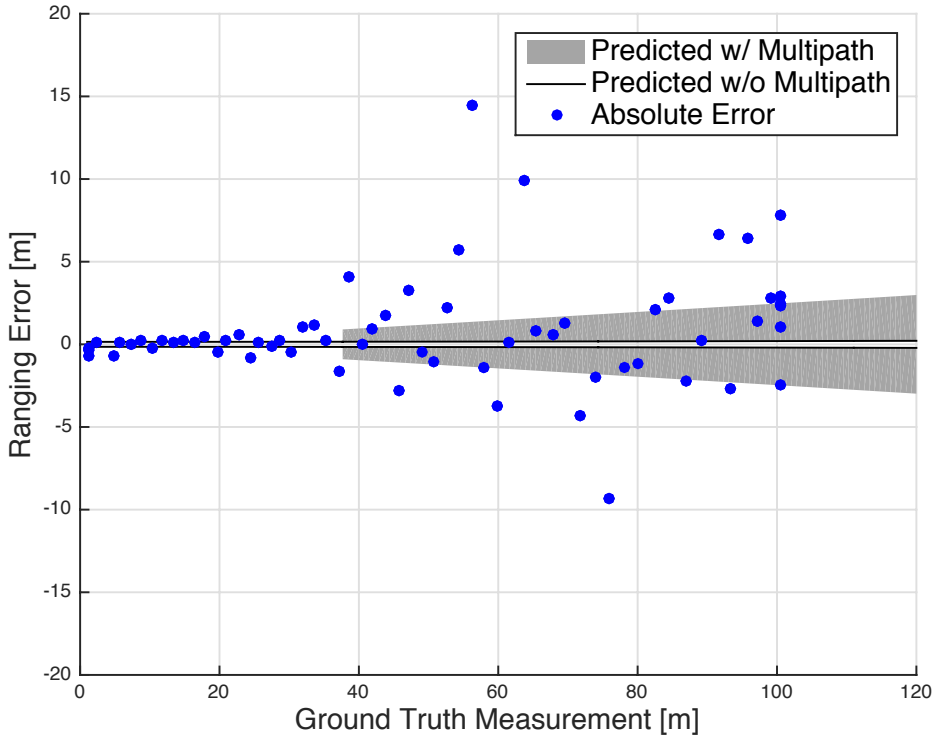

Fig. 9 Range measurement error for the dynamic trial, where the line represents the predicted one-sigma error with no multipath interference, and the shaded region represents all of the possible one-sigma errors given multipath interference

5 Range Error Model

A key contribution of this work is to develop error models to describe the phenomena observed in experimental trials and to predict the performance of our equipment over distances larger than supported by our test facility.

Range measurement error is assumed to be composed primarily of two independent sources: timing error from imperfect clocks and tracking error from noise and multipath signals. Assuming Gaussian errors, the total one-sigma range measurement error σ_r is the root of the sum of the squares of the one-sigma clock error $\sigma_{r,clk}$ and the one-sigma tracking error $\sigma_{r,tr}$

$$\sigma_r = \sqrt{\sigma_{r,clk}^2 + \sigma_{r,tr}^2}. \tag{10}$$

5.1 Clock Error

Clock error results from uncertainty in the limited time resolution of DAQ, which acquired samples from both the arbitrary waveform generator clock and the detector. The sample interval was 1 ns, and sampling was phase locked with the modulation frequency. Because of discrete sampling, the relative phase of the transmitter and receiver signals cannot be determined with a resolution of better than half a sample. Taking clock error to be 0.5 ns one-sigma, and multiplying by the speed of light c results in a clock ranging error $\sigma_{r,clk}$ of 15 cm, one-sigma, in Eq. (10).

5.2 Tracking Error

In addition to clock error, tracking error is a significant contributor to the total range measurement error. The one-sigma tracking error $\sigma_{r,tr}$ primarily depends on the ability of the integrators in Eqs. (6) and (7) to pick out the

signal over the background noise. In other words, accuracy is a function of the received code-to-noise power ratio C/N. A model of the one-sigma error $\sigma_{r,tr}$ in Eq. (10), as a function of the code-to-noise ratio C/N, is derived in the Appendix. The primary result of this derivation, where c is the speed of light and ω is the angular frequency of the modulated signal, is

$$\sigma_{r,tr} = \frac{c}{\omega}\sqrt{\frac{1}{2(C/N)}}. \tag{11}$$

The code-to-noise ratio C/N is the key parameter in this expression. It compares the power of the desired signal C to the power of the background noise N. It varies with the distance between the transmitter and receiver as the strength of the signal decreases. To develop a representative model of the error, we consider two distinct regions: short distances where only the direct signal and thermal noise reach the receiver, and long distances where indirect multipath signals (i.e. signals that reflect off the ground) must also be considered (as shown in **Fig. 10**).

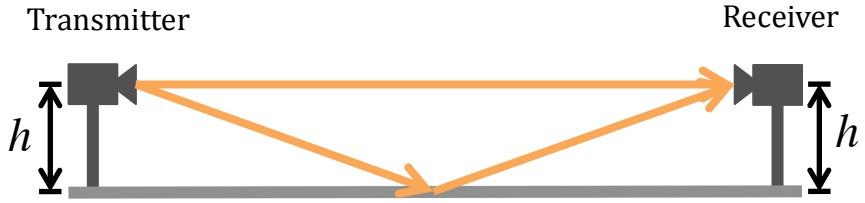

Fig. 10 The direct signal travels along a straight path between the transmitter and receiver, while the indirect multipath signal bounces off a surface (in this case the ground)

5.2.1 Direct Signal

To develop a model of the code power C_d in the absence of multipath, consider the system link budget. After accounting for all losses, the received signal power C_d is only a fraction of the initial transmitted power P_T. The dominant energy loss is due to beam spreading. Spreading losses are calculated as the ratio of the area of the receiver lens A_{lens} to the area $2\pi r^2(1-\cos\phi_t)$ of the spherical cap subtended by the beam (the spatial propagation pattern of the beam is spherical), which is a function of range r from the transmitter and beam spreading angle ϕ_t. In the terahertz regime, the beam is also scattered as it travels through the atmosphere. Scattering losses are exponential as a function of range, as expressed in terms of an atmospheric attenuation coefficient α. Combining these losses, and treating the transmitter as a far field point source such that the waves can be assumed to travel as concentric spherical caps, the received code power is expressed as

$$C_d = P_T \cdot \rho_{processing}\left(e^{-\frac{\alpha r}{10}\ln 10}\right)\frac{A_{lens}}{2\pi r^2(1-\cos\phi_t)}. \tag{12}$$

Signal processing incurs additional losses, as accounted for by $\rho_{processing}$. The on-off modulation of the transmitted signal shifts only half of the transmitted power to the baseband. Of the remaining signal power, only a fraction $8/\pi^2$ resides in the fundamental frequency of the transmitted square wave. The rectification process acts like multiplication by a square wave in the time domain (or a convolution in the frequency domain), such that the fundamental frequency power is again spread through the harmonics of a square wave, again reducing power in the fundamental frequency (post-rectification) by $8/\pi^2$. Combining these three multipliers, the net result is a signal processing loss $\rho_{processing}$ equal to $32/\pi^4$ (or about 0.33).

The code power from the direct signal is balanced against the noise power N at the fundamental frequency in Eq. (11). Background noise comes from environmental radiation and from the receiver electronics. Based on our assumption that the noise is white, the noise spectral density N_0 is essentially uniform across a broad range of frequencies. The total noise power received is the product of the noise spectral density and detector bandwidth B_N, but this power is divided among K discrete frequencies when frequency-domain analysis is applied to K points. Hence the noise in the discrete band associated with the fundamental frequency is N, where

$$N = \frac{B_N N_0}{K}. \tag{13}$$

In our experiments, *C*/*N* was determined directly from the data, as described in the results section above. For a known value of code power computed by (12), the noise N at each discrete frequency was determined experimentally to be $N \approx 1.1\times10^{-11}$ W.

5.2.2 Multipath Effects

Though multipath was not a factor at short ranges, multipath became important at ranges beyond about 37 m. To understand this sudden onset of multipath, consider the equipment geometry shown in **Fig. 11**. Both the transmitter and receiver have relatively narrow beam angles over which they can transmit or receive signal. Assume that the lenses give each beam pattern a sharp rolloff, going quickly from a maximum value to zero near the edge of the beam. As a result of this assumption, the signal from the transmitter that reaches the ground is essentially zero out to a distance a_t from the transmitter base. The distance a_t depends on the transmitter height h and the beam angle ϕ_t.

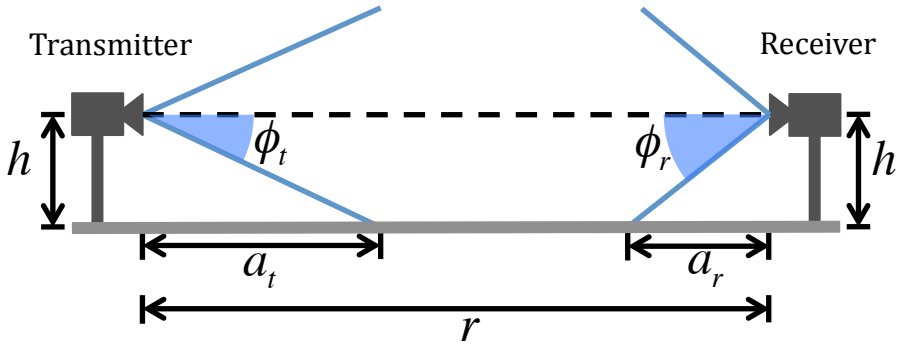

Fig. 11 The transmitter and receiver geometry

Similarly, the closest distance over which the receiver can see a signal from the ground is a distance a_r away from its base. Thus for this model, no indirect multipath signal is visible at the receiver for equipment separations shorter than the sum $a_t + a_r$. For distances greater than the sum $a_t + a_r$, on the other hand, both the direct signal and the indirect multipath signal reflected from the ground reach the receiver. This means that for long distances, the power of the transmitted signal must be modified to account for indirect multipath. The sum $a_t + a_r$ is approximately 37 m for the parameters of the hardware system used in this work.

The power C_{mp} of the multipath signal is modeled in a similar manner to the direct signal power shown in Eq. (12), with two key differences. First, the distance r_{mp} that the multipath signal travels is slightly longer than the distance r that the direct signal travels. This difference in path length is small, and therefore results in a negligibly small change in the power. The second difference is that not all of the power will be reflected by the surface, as encompassed by the coefficient of reflectivity ρ_{ref}. The multipath signal power is thus given as

$$C_{mp} = P_T \cdot \rho_{ref} \cdot \rho_{processing} \left(e^{-\frac{\alpha r_{mp}}{10}\ln 10}\right) \frac{A_{lens}}{2\pi r_{mp}^2 (1-\cos\phi_t)}. \tag{14}$$

Because of the relative infancy of THz technology, the coefficient of reflectivity ρ_{ref} has not been well characterized for most materials. A study [31] of THz reflections off common (relatively smooth) building materials including glass, plaster, and wood found coefficients of reflectivity approaching 1 as the angle of incidence approached 90° (near grazing). Considering that the angle of incidence is slightly less than 90° in our case and the asphalt surface has roughness on the order of the wavelength (1 mm) making reflections a little more diffuse, we selected a reflectivity slightly less than this ideal value of unity (namely, $\rho_{ref} = 0.9$, a value which agrees reasonably well with our experimental results).

In typical radionavigation applications like GPS, the main impact of multipath signals is to bias distance measurements due to the additional path length of the reflected signal. In our case, the maximum additional path length of a multipath signal is about 5.7 cm. This results in a maximum bias of only 2.85 cm, which is significantly less than the clock error of 15 cm, and therefore not a significant contributor to the overall error.

The multipath signal, however, has another effect. Consider the two-ray model [32,33]. In this model, the primary impact of the multipath signal is to interfere, either constructively or destructively, with the carrier waves of the direct signal. This interference alters the signal strength, either increasing or decreasing the signal-to-noise ratio. This means that depending on the precise geometry of the equipment and the resulting carrier phase difference, the multipath signal can improve or degrade the accuracy of the range measurements.

Because of the short wavelength of the THz carrier signal (1 mm), very small changes in the path length will result in significant changes in the phase difference between the multipath and direct signals. In addition, the point of reflection can vary significantly because the ground surface, an asphalt parking lot, is composed of many smooth surfaces oriented at various angles. Any change in the equipment position due to bumping, wind, or wobbling may result in a significant change in the relative path lengths, causing a transition between constructive and destructive interference. Similarly, sub-mm shifts in the phase center of the transmitting and/or receiving antenna due to thermal effects can also affect the interference pattern. Because of this high sensitivity, we model the amount of interference between the direct and indirect signals as essentially random between two extremes (fully constructive and fully destructive interference). Fully constructive interference results in an effective boost to the signal code power at the receiver, while destructive interference results in an effective decrease of the signal power. Equation (15) computes these upper and lower bounds, C_{max} and C_{min}, noting that power is amplitude squared

$$C_{max} = \left(\sqrt{C_d} + \sqrt{C_{mp}}\right)^2$$
$$C_{min} = \left(\sqrt{C_d} - \sqrt{C_{mp}}\right)^2. \quad (15)$$

Fig. 12 shows the effects of multipath on C/N. The modeled signal-to-noise ratio for the direct signal (black line) is high at short ranges *r* but decreases as *r* increases, since code power is a function of *r* while thermal noise is not. There are no multipath signals at short range; however, at approximately 37 m, the multipath signals come into play, and constructive and destructive interference are both possible. This is represented by the gray region. If the level of multipath interference is essentially random, then the signal-to-noise ratio can take any value in the gray region. In the constructive interference case (top of the gray region), C/N increases slightly relative to the direct signal. In the case of destructive interference (bottom of the gray region), C/N is significantly decreased.

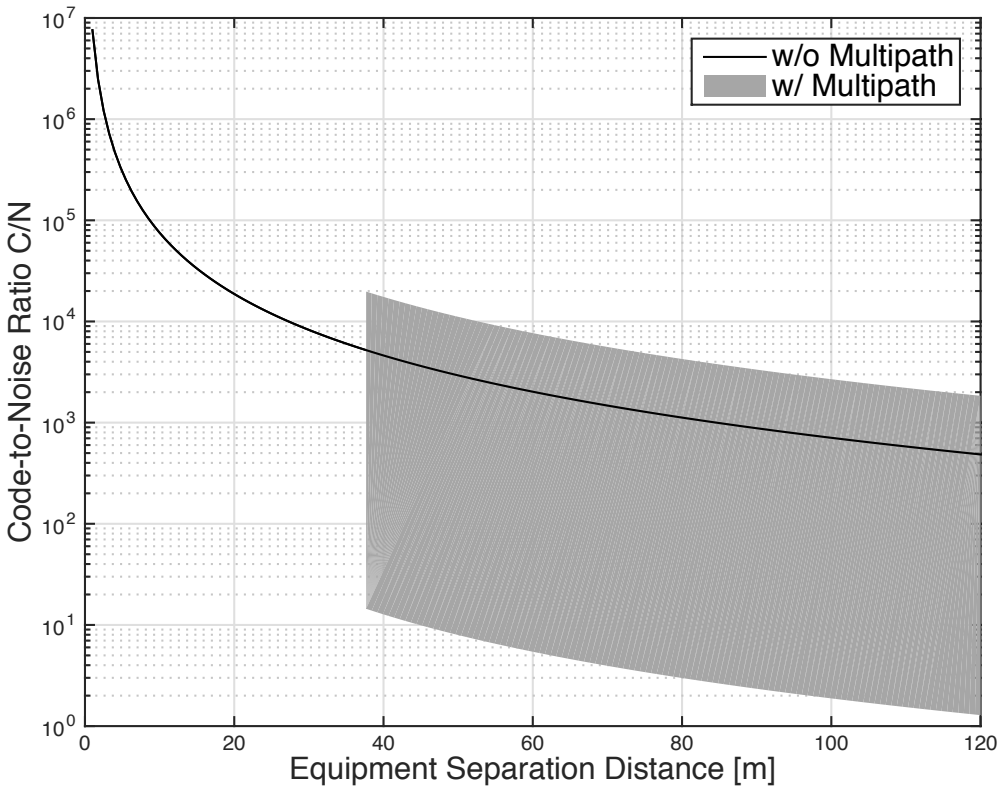

Fig. 12 Modeled signal-to-noise ratio v. transmission distance, where the black line shows the ratio when there is no multipath interference and the gray area shows the range of possible values that result from multipath interference

The *C*/*N* values plotted in **Fig. 12** were generated using parameter values listed in **Table 1**. The thermal noise N_0 was determined from experimental data, as described in the Thermal Noise Measurement section below. We did not have experimental data for ground reflectivity $\rho_{reflection}$, so it was used as a tuning parameter to set the noise level in the static trial, as described in the Results section below. All other parameters were obtained from system specifications or, for parameters describing the natural world, from standard tabulated data.

Table 1 Parameters that affect the signal-to-noise ratio

Parameters Affecting Range Error	
Carrier frequency	0.3 THz
Speed of light c	3.0×10^{8} m/s
Atmospheric attenuation α	3 dB/km
Ground Reflectivity $\rho_{reflection}$	0.9
Thermal noise N_0	5.9×10^{-15} W/Hz
Noise bandwidth B_N	1 GHz
Angular frequency ω	$2\pi\times10$ MHz
Transmitted power P_T	30 mW
Lens area A_{lens}	4.9×10^{-5} m^2
Transmitter spreading angle ϕ_t	2.5°
Receiver spreading angle ϕ_r	4°
Equipment height h	1 m
Buffer length K	450,000 pts

6 Discussion

The primary challenge in adapting GPS ranging techniques to THz frequencies is the current inability of THz hardware to track the signal's carrier phase. As a result, simple on-off keying is used to modulate the carrier signal instead of BPSK, resulting in a power loss as half of the power drops to DC. As THz technology matures, it is expected that carrier phase tracking may become available. In addition to BPSK, this capability would enable carrier phase smoothing methods used in GPS, like Hatch filtering [8]. Because of their short wavelength, THz signals could provide extremely precise range measurements using these methods.

The trials described above demonstrate accurate THz range measurements at the limit of our current test range. In the static case, even with relatively severe multipath interference, measurements of up to 100 m are demonstrated with only a couple meters of error (one-sigma). The significant increase in error in the dynamic trial is likely the result of small bumps and rotations of the transmitter cart as it was manually pulled backward. These resulted in slight misalignments of the transmitter and receiver equipment. Because of the tight beam patterns, even small misalignments could result in significant decreases in the code-to-noise ratio, and corresponding degradation of the measurement accuracy. The dynamic trials may also be affected by Doppler shift, which was assumed to be zero for this system, or by secondary multipath.

We also note the particular sensitivity of THz signals to multipath interference. When ground-bounce multipath is present, the short wavelength of THz signals combined with the rough asphalt surface of the test range cause the received signal to transition somewhat unpredictably between regions of constructive and destructive interference for even very small changes in equipment configuration. This phenomenon is both a mathematical consequence of our error modeling and a reasonable description of our experimental observations, where measurement errors jump suddenly at the distances where multipath is active (40 m).

The multipath model presented in this paper describes a single reflection from the horizontal ground surface; however, signal reflections from vertical reflectors on the edges of the test range (e.g. cars or sign posts in the parking lot) may have resulted in additional secondary multipath interference. For certain equipment geometries, these additional paths could act to effectively concentrate interference on the receiver. Although we did our best to avoid secondary multipath, this may explain the outlier data points observed in both the static and dynamic trials at roughly 50 m separation.

The ground-bounce multipath model presented has a couple of interesting consequences. First, as long as multipath signals are a factor, simply increasing the transmitter strength will not significantly improve the signal-to-noise ratio. As the direct signal strength increases, the multipath signal strength will increase alongside it. Second, the model also suggests that a thoughtful system design modification (e.g.increasing the height of the equipment or narrowing the transmitter beam) could significantly mitigate multipath. Such mitigation could enable accurate THz ranging over much longer distances than those of our experimental demonstrations. Our error models, given by Eqs.

(10)-(13), predict that in the absence of multipath interference range measurements over a 1 km baseline would result in measurement errors of only 1.76 m one-sigma. Verifying this prediction is an important topic for future work.

Other system design features might be adjusted to increase accuracy. A key user defined design parameter is the integrator buffer length K in Eqs. (6) and (7), which can be tuned to mitigate noise. Larger values of K provide more filtering and hence more noise mitigation. In the longer term, enhanced THz electronics could also improve system accuracy, particularly if it were feasible to employ Phase Shift Keying (PSK) and Quadrature Amplitude Modulation (QAM) as is common in radio communications.

7 Summary

This paper introduces a novel THz ranging system, modeled on GPS systems, which uses a 300 GHz carrier signal modulated with a simple 10 MHz square wave. Experiments successfully obtained measurements with decimeter accuracy up to 40 m range, and with approximately 10 m accuracy at 100 m range. An error model was developed that well characterized experimental results. The error model suggests that tracking errors due to thermal noise are very low at the ranges tested. For the system described herein, clock sampling errors were dominant below distances of about 40 m, and multipath errors were dominant at longer distances.

8 Appendix

This appendix provides a derivation of the range measurement error expression given in Eq. (11). It begins with a model of the primary sinusoidal component of the continuous time signal detected by the receiver, where C is the signal power and $n(t)$ is noise

$$v_r = \sqrt{C}\cos(\omega t + \theta) + n(t). \tag{16}$$

The goal is to find the phase shift θ. To do this, the signal is compared to a replica signal $\hat{v}_r$ in the integrators shown in Eqs. (6) and (7),

$$\hat{v}_r = \cos(\omega t). \tag{17}$$

Discretizing the signal model and plugging in, the in-phase integrator from Eq. (6) is given as

$$I_i(k) = \sum_{m=k-K+1}^{k} v_r \hat{v}_r = \sum_{m=k-K+1}^{k} \left(\sqrt{C}\cos(\omega m\tau + \theta) + n(t)\right)\cos\omega m\tau. \tag{18}$$

With the help of some trigonometric identities, this expression can be re-arranged as follows,

$$I_i(k) = \sum_{m=k-K+1}^{k} \frac{\sqrt{C}}{2}\cos\theta + \sum_{m=k-K+1}^{k} \frac{\sqrt{C}}{2}\cos(2\omega m\tau + \theta) + \sum_{m=k-K+1}^{k} n_m\cos(\omega m\tau). \tag{19}$$

The first term of Eq. (19) is simple to evaluate. Because the terms of the summation do not depend on the summation variable m, it is the summation of K equal terms and the summation can be replaced by multiplication by K. The second term will be zero, because the buffer size used in this work is an integer multiple of the number of samples per modulation period, leaving

$$I_i(k) = \frac{K\sqrt{C}}{2}\cos\theta + \sum_{m=k-K+1}^{k} n_m\cos(\omega m\tau). \tag{20}$$

For the final term, the noise per Fourier frequency bin n_m must be modeled. For white noise, the power is uniformly distributed across the bins, so the power in any one bin is N. As a result, we have the following continuous time model of the noise per bin n_m, where $\tilde{\theta}$ is the random phase of the noise signal

$$n_m(t) = \sqrt{N}\cos\left(\omega t + \tilde{\theta}_l\right). \tag{21}$$

Now, this expression is plugged into Eq. (20) and again a trigonometric identity is applied to give

$$\sum_{m=k-K+1}^{k} n_m \cos(\omega m\tau) = \sqrt{N}\left(\sum_{m=k-K+1}^{k} \frac{1}{2}\cos\tilde{\theta} + \sum_{m=k-K+1}^{k} \frac{1}{2}\cos\left(2\omega m\tau + \tilde{\theta}\right) \right). \tag{22}$$

Using the same arguments as above, the summation on the first term can be replaced by multiplication by K, and the second summation goes to zero leaving

$$\sum_{m=k-K+1}^{k} n_m \cos(\omega m\tau) = \frac{K}{2}\sqrt{N}\cos\tilde{\theta}. \tag{23}$$

The in-phase component of the signal is thus reduced to the equation below. Likewise, the quadrature component is found using the same process except that sine is used in the replica signal instead of cosine (i.e. $\hat{v}_r = \sin(\omega t)$)

$$\begin{aligned} I_i(k) &= \frac{K\sqrt{C}}{2}\cos\theta + \frac{K}{2}\sqrt{N}\cos\tilde{\theta} \\ Q_i(k) &= -\frac{K\sqrt{C}}{2}\sin\theta - \frac{K}{2}\sqrt{N}\sin\tilde{\theta}. \end{aligned} \tag{24}$$

To find the error in the phase angle estimate $\hat{\theta}$ relative to the actual angle θ, shift the angle coordinate (without loss of generality) and apply the inverse tangent operation

$$\tan\left(\hat{\theta} - \theta\right) = \frac{\sqrt{N}\sin\tilde{\theta}}{\sqrt{C} + \sqrt{N}\cos\tilde{\theta}}. \tag{25}$$

The geometric interpretation of this is shown graphically in **Fig. 13**.

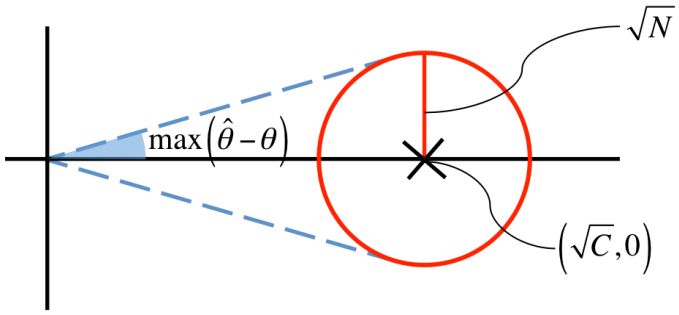

Fig. 13 Geometric interpretation of integrator error

Because white noise is assumed, the unknown phase $\tilde{\theta}$ is evenly distributed and so (25) represents a circle around the point $\left(\sqrt{C},0\right)$ with radius $\sqrt{N}$.

Assuming that $\sqrt{C} \gg \sqrt{N}$ and making the small angle approximation, the equation can be simplified to

$$\hat{\theta} - \theta = \sqrt{\frac{N}{C}}\sin\tilde{\theta}. \tag{26}$$

The variance of a uniform distribution $\tilde{\theta}$ mapped through the function $\sin\tilde{\theta}$ is ½. Hence the phase-jitter has variance σ_θ^2, which can be computed as the variance of Eq. 26,

$$\sigma_\theta^2 = \mathrm{var}\left(\hat{\theta} - \theta\right) = \frac{1}{2}\frac{N}{C}. \tag{27}$$

Converting from phase-jitter to range measurement error in units of distance requires scaling by the speed of light c and the angular frequency of the modulation signal ω

$$\sigma_r = \frac{c}{\omega}\sigma_\theta = \frac{c}{\omega}\sqrt{\frac{1}{2(C/N_0)}}. \quad (28)$$

Acknowledgements Many thanks to the Air Force Research Laboratory who supported this work through contract FA8650-12-C-3204.

References

1. N. D. Pham, *The Economic Benefits of Commercial GPS Use in the U.S. and The Costs of Potential Disruption* (NDP Consulting Group, 2011).
2. John A. Volpe National Transportation System Center, *Vulnerability Assessment of the Transportation Infrastructure Relying on the Global Positioning System* (U.S. Department of Transportation, 2001).
3. S. Pullen and G. X. Gao, Inside GNSS **7**, 34 (2012).
4. S. Lo, Y.-H. Chen, and P. Enge, in *Proceedings of the 28th International Technical Meeting of The Satellite Division of the Institute of Navigation (ION GNSS+ 2015)* (Tampa, FL, 2015), pp. 1468–1477.
5. T. Ertan and M. L. Psiaki, in *Proceedings of the 27th International Technical Meeting of The Satellite Division of the Institute of Navigation (ION GNSS+ 2014)* (Tampa, FL, 2014), pp. 3055–3064.
6. J. S. Parker, Terahertz-Based Relative Positioning of Aircraft Flying in Formation, M.S. Thesis, Tufts University, 2013.
7. J. S. Parker and J. Rife, in *Proceedings of the ION 2013 Pacific PNT Meeting* (Honolulu, Hawaii, 2013), pp. 811–821.
8. H. K. Lee and C. Rizos, IEEE Transactions on Aerospace and Electronic Systems **44**, 30 (2008).
9. P. Misra and P. Enge, *Global Positioning System: Signals, Measurements and Performance Second Edition* (Lincoln, MA: Ganga-Jamuna Press, 2011).
10. E. Bründermann, H.-W. Hübers, and M. F. Kimmitt, *Terahertz Techniques* (Springer, Berlin, 2012).
11. Y.-S. Lee, *Principles of Terahertz Science and Technology* (Springer, 2009).
12. G. P. Williams, Rep. Prog. Phys. **69**, 301 (2006).
13. G. A. Siles, J. M. Riera, and P. García-del-Pino, in *Antennas and Propagation (EuCAP), 2010 Proceedings of the Fourth European Conference on* (IEEE, 2010), pp. 1–5.
14. M. Cooke, III-Vs Review **19**, 36 (2006).
15. T. Kleine-Ostmann and T. Nagatsuma, J Infrared Milli Terahz Waves **32**, 143 (2011).
16. X. Mei, W. Yoshida, M. Lange, J. Lee, J. Zhou, P. H. Liu, K. Leong, A. Zamora, J. Padilla, S. Sarkozy, R. Lai, and W. R. Deal, IEEE Electron Device Letters **36**, 327 (2015).
17. A. J. Fitzgerald, V. P. Wallace, M. Jimenez-Linan, L. Bobrow, R. J. Pye, A. D. Purushotham, and D. D. Arnone, Radiology **239**, 533 (2006).
18. B. Hussain, M. Ahmed, M. Nawaz, M. Saleem, M. Razzaq, M. Aslam Zia, and M. Iqbal, Appl. Opt. **51**, 5326 (2012).
19. T. Yasui, Y. Kabetani, Y. Ohgi, S. Yokoyama, and T. Araki, Appl. Opt. **49**, 5262 (2010).
20. M. Caris, S. Stanko, A. Wahlen, R. Sommer, J. Wilcke, N. Pohl, A. Leuther, and A. Tessmann, in *2014 11th European Radar Conference (EuRAD), 8-10 Oct. 2014* (IEEE, 2014), pp. 494–6.
21. N. Pohl, S. Stanko, M. Caris, A. Tessmann, and M. Schlechtweg, in *2015 IEEE Topical Conference on Wireless Sensors and Sensor Networks (WiSNet), 25-28 Jan. 2015* (IEEE, 2015), pp. 62–4.
22. W. R. Tribe, D. A. Newnham, P. F. Taday, and M. C. Kemp, in (2004), pp. 168–176.
23. M. Salhi, T. Kleine-Ostmann, M. Kannicht, S. Priebe, T. Kürner, and T. Schrader, in *Microwave Conference Proceedings (APMC), 2013 Asia-Pacific* (2013), pp. 1109–1111.
24. M. Salhi, T. Kleine-Ostmann, T. Schrader, M. Kannicht, S. Priebe, and T. Kurner, in *Microwave Conference (EuMC), 2013 European* (2013), pp. 175–178.
25. J. Federici and L. Moeller, Journal of Applied Physics **107**, 111101 (2010).
26. C. Han and I. F. Akyildiz, in *2014 IEEE International Conference on Communications (ICC)* (2014), pp. 5461–5467.
27. C. Jastrow, K. Munter, R. Piesiewicz, T. Kurner, M. Koch, and T. Kleine-Ostmann, Electronics Letters **44**, 213 (2008).

28. C. Jastrow, S. Priebe, B. Spitschan, J. Hartmann, M. Jacob, T. Kurner, T. Schrader, and T. Kleine-Ostmann, Electronics Letters **46**, 661 (2010).
29. D. R. Vizard, M. Gashinova, E. G. Hoare, and M. Cherniakov, in *16th International Radar Symposium, IRS 2015, June 24, 2015 - June 26, 2015* (IEEE Computer Society, 2015), pp. 209–214.
30. P. Dzwonkowski, P. Samczynski, K. Kulpa, J. Drozdowicz, D. Gromek, and P. Krysik, in *Signal Processing Symposium (SPSympo), 2015* (2015), pp. 1–5.
31. R. Piesiewicz, T. Kleine-Ostmann, N. Krumbholz, D. Mittleman, M. Koch, and T. Kurner, Electronics Letters **41**, 1002 (2005).
32. S. Loyka and A. Kouki, IEEE Antennas and Propagation Magazine **43**, 31 (2001).
33. S. Priebe, C. Jastrow, M. Jacob, T. Kleine-Ostmann, T. Schrader, and T. Kurner, IEEE Transactions on Antennas and Propagation **59**, 1688 (2011).